Polymorphous band structure model of gapping in the antiferromagnetic and paramagnetic phases of the Mott insulators MnO, FeO, CoO, and NiO

Giancarlo Trimarchi, Zhi Wang, and Alex Zunger

Phys. Rev. B **97**, 035107 — Published 5 January 2018

DOI: 10.1103/PhysRevB.97.035107

A polymorphous band structure description of gapping in the antiferromagnetic and paramagnetic phases of the Mott insulators MnO, FeO, CoO, and NiO

Giancarlo Trimarchi [(1)] Zhi Wang [(2)] and Alex Zunger [(2)]

(1) Department of Chemistry, Northwestern University, Evanston, Illinois 60208, USA

(2) Renewable and Sustainable Energy Institute, University of Colorado, Boulder, Colorado 80309, USA

The existence of band gaps in both the antiferromagnetic (AFM) and paramagnetic (PM) phases of the classic NaCl-structure Mott insulators MnO, FeO, CoO, and NiO is traditionally viewed and taught as a manifestation of strong correlation whereby insulation results from electrons moving across the lattice forming states on certain atomic sites with doubly occupied *d* orbitals and empty *d* orbitals on other sites. Within such theories, the gap of the AFM and PM phases of these oxides emerges even in the absence of spatial symmetry breaking. The need for such a correlated picture is partially based on the known failure of the commonly used band models for the PM phase which assumes for such a spin disordered state the macroscopically averaged NaCl structure, where all transition metal (TM) sites are symmetry-equivalent (a *monomorphous* description), producing a gapless PM state with zero magnetic moments, in sharp conflict with experiment. Here we seek to understand the *minimum theoretical description* needed to capture the leading descriptors of ground state Mott insulation in the classic, 3d monoxide Mott systems—gapping and moment formation in the AFM and PM. As noted by previous authors, the *spin-ordered* AFM phases already show in band theory significant band gaps when one doubles the NaCl unit cells by permitting different potentials for transition metal atoms with different spins. For the *spin-disordered* PM phase we allow analogously larger NaCl-type supercells where each TM site can have different spin direction and local bonding environments (i.e. disordered), yet the total spin is zero. Such a *polymorphous* description has the flexibility to acquire symmetry-breaking energy lowering patterns that can lift the degeneracy of the *d* orbitals and develop large on-site magnetic moments without violating the global, averaged NaCl symmetry. Electrons are exchanged between spin up and spin down bands to create closed shell insulating configurations that lend themselves to a single determinental description. It turns out that such a polymorphous description of the structure within the single determinant, mean field, Bloch periodic band structure approach (based on DFT+U) allows large on-site magnetic moments to develop spontaneously, leading to significant (1-3 eV) band gaps and large local moments in the AFM, and PM phases of the classic NaCl-structure Mott insulators MnO, FeO, CoO, and NiO in agreement with experiment. We adapt to the spin disordered polymorphous configurations the "special quasi-random structure" (SQS) construct known from the theory of disordered substitutional alloys whereby supercell approximants which represent the best random configuration average (not individual snapshots) for finite (64, 216 atoms or larger) supercells of a given lattice symmetry are constructed. We conclude that the basic features of these paradigm Mott insulators can be approximated by the physics included in symmetry broken DFT.

Email: gtrimarc@gmail.com, alex.zunger@colorado.edu

I. Introduction

The physical origin of the insulating phases occurring in crystals with partially occupied *d* shells exemplified by the transition metal (TM) monoxides MnO, FeO, CoO and NiO, has held the condensed matter physics community in constant fascination ever since Mott and Peierls proposed an explanation[1]. These oxides have a low-temperature spin-ordered antiferromagnetic (AFM) phase, in which they exhibit slightly distorted rock salt structures (rhombohedral for NiO, and MnO, and monoclinic for CoO and FeO, the latter having also Jahn Teller atomic displacements), and a high-temperature spin disordered paramagnetic (PM) phase, having macroscopically the cubic rock salt structure and a globally zero magnetic moment. In simplified band structure calculations[2-7] it has been customary to evaluate the electronic structure for the macroscopically observed average rock salt configuration $\mathbf{\Sigma}_0$. Because there is but a single transition metal atom in such a unit cell, the PM condition of globally zero magnetic moment leads to vanishing local magnetic moment $\mu_i(\mathbf{\Sigma}_0)$ at *each metal site* i, and therefore, by symmetry, to zero band gaps $E_g(\mathbf{\Sigma}_0)$ for such odd number of electron cases. Here, $\mathbf{\Sigma}_0$ was taken as the non-magnetic, cubic rock salt configuration in which all TM sites are equivalent (a *monomorphous* representation). As is generally taught[8, 9] , the ensuing electronic structure of compounds having partially occupied energy bands described in a structure where all atoms are equivalent would be metallic[2, 3] with the Fermi level intersecting a band. Yet, experimentally MnO, FeO, CoO and NiO are local-moment large band gap insulators, both in the AFM and PM phase[10-12] (see Table I).

The fundamental disagreement between such band structure theory and experiment set the historical stage for modeling the electronic structure of the PM phases of MnO, FeO, CoO and NiO and related quantum materials by many-body, correlated electron descriptions, such as the description based on the Hubbard Hamiltonian[13, 14], or, more recently, the dynamical mean field theory (DMFT)[15, 16] rendering of the Hubbard Hamiltonian. Within such theories, the gap of the AFM and PM phases of these oxides emerges because the *d* electrons become localized due to the correlation-induced electron-electron repulsion, even in the absence of spatial symmetry breaking (symmetry can break afterwards, as a secondary fact). From the strongly correlated standpoint the existence of local magnetic moments is a consequence of the electron localization and not an essential part of the gap opening mechanism itself. The Mott mechanism envisions that the electrons move across the lattice forming states on certain atomic sites with doubly occupied *d* orbitals and empty *d* orbitals on other sites. These types of excited configurations correspond respectively to the upper and lower Hubbard bands, which are envisioned to form the physical band edges ,i.e the valence band maximum and conduction band minimum.

Indeed one often finds in the literature comments that single determinant mean field DFT band theory fails to reproduce the gap in the absence of long-range magnetic order.[4, 17-19] But such conclusions may have been clouded by a few restrictions applied unwittingly to band theory itself. For example, the model that has been often used for the PM phase of these oxides restricts

all metal sites to see identical local environments and potentials, ie use unit cells with single TM per cell. Because such a monomorphous representation of a disordered PM phase forces upon us in band theory a zero magnetic moment *on an atom-by-atom* basis (instead of having a global zero moment but nonzero local moments), the ensuing band gaps in such nonmagnetic models were always zero, irrespective of the quality of the description of the interelectronic interaction $E_{xc}[n^{\uparrow}(\mathbf{r}), n^{\downarrow}(\mathbf{r})]$ in DFT band theory. However, as shown here, upon examining the total DFT energies, one finds that the non magnetic (NM) 'phase' is unstable by more than 2 eV/formula unit than a proper DFT paramagnetic phase of CoO, so the NM it is but an hypothetical state. In addition to confusing paramagnetic state with non magnetic state, other approximation to DFT band theory may have perhaps prematurely disqualified such approaches for describing even simple Mott systems and related quantum materials. These include (i) disallowing geometrical symmetry breaking (such as Jahn –Teller, or atom-pairing, or charge disproportionation), or (ii) using DFT functionals that do not distinguish occupied from unoccupied states (ie lacking exchange correlation discontinuity as in self interaction corrected DFT or its DFT+U approximant), thus forcing equal and fractional occupation of all components of open shell degenerate states at the Fermi energy. Since none of these simplifications are defining features of band theory itself, the failure of such approaches in explaining Mott insulation may have been prematurely viewed as a fundamental failure of the single determinant mean field approach itself. The path then suggested in the literature to model the paramagnetic state of Mott insulators has been that of solving the Hubbard model by strongly correlated approaches. (Perhaps an early clue that d electron strong correlation is not the deciding factor for these binary oxide systems is the fact that the valence band and conduction band edges consist of oxygen p and transition metal s orbitals, shown below, not the proverbial d-like lower and upper Hubbard bands, envisioned by the founding thinkers in this field). Here, we relax the restrictions often imposed previously but which are not an integral part of band theory per se, *seeking to understand the minimum theoretical approach needed to describe the leading features of the Mott insulating behavior*, namely, gap opening and amplitude and on-site magnetic moment formation in the AFM and PM phase of the classic, 3d monoxide Mott systems. To this end we deliberately use a single-determinant, mean field Bloch periodic band structure approach (based on DFT+U), but permit any energy-lowering symmetry breaking effects sanctioned by such a mean field description.

We find here for the text book MnO, FeO, CoO and NiO Mott insulators that symmetry breaking afforded by using in band theory sufficiently flexible unit cells (the polymorphous representation of disorder) and allowing orbital occupation symmetry breaking and spin unrestricted symmetry breaking produce in DFT+U [20-24] an insulating solution (band gaps of 1-3 eV) with strong local magnetic moments (2-4 Bohr Magnetons), in general agreement with experiment. This symmetry breaking is not assumed, but obtained as an energy-lowering event within the mean field like variational theory, and differs from correlation-induced gap opening mechanism in the absence of spatial symmetry breaking. This approach produces detailed geometrical information (such as atomic displacements; equilibrium cell structure), magnetic

moments, band gaps, bonding charge density, and the total energies of al phases, and permits the future use of precisely the same polymorphous description for studying defects and doping. The emerging physical picture is that at any given moment in time, (i.e., a snapshot) each TM atom will have a finite magnetic moment (but randomly pointing to different directions), and these moments are rotating with time. So, the average magnetic moment of each atom will not equal to zero because of a quantum fluctuation. The conventional physics encoded in DFT with current nonlocal functionals-- bonding, magnetism, spin-polarization, Jahn-Teller distortions, hybridization and selective occupation of the components of e_g and t_2 orbitals --suffices to produce large moments if not disallowed by imposing artificially high symmetry. As a result of these symmetry-breaking channels, electrons are exchanged between spin up and spin down bands to create insulating closed shell configuration that lend them to a single determinental description. Whereas the final expression would involve a (macroscopically symmetrized) combination of all individual symmetry broken configuration, *the crucial fact is that such individual symmetry broken configuration have closed shells with large band gaps and magnetic moments*, suggesting that such configurations would have but weak mutual interaction, so dynamically correlated approaches are not forced upon us by the physics at hand. We note that it is entirely possible that some *other* Mott compounds would remain metallic in a single particle treatment even if the monomorphous description were replaced by a polymorphous representation. It is also possible that DFT with the current functional could miss properties *other* than the insulating character of the PM phases. We are not claiming otherwise. These are open, future research questions.

The fact that the main attribute of the classic Mott insulators (i.e., the existence of gaps) could be described by mean-field, single configuration band theory is consequential, as it redefines the minimal level of physics and computational effort required. Indeed, such single determinant mean field like DFT approaches have recently successfully described in agreement with experiment the hole density in p-type doped NiO (ref [25]), the metal-insulator transition in rare earth nickelates (ref [26]), and the n-type doping of SmNiO3 (Ref [27]), discussed in Ref [28]. Such results may open the door for reexamination of the utility of non naïve DFT based band theory methods for studying the basic attributes of more complex Mott systems, including ternary and quaternary oxides, as well as defects, doping, and interface characteristics.

II. Dual inputs to electronic structure theory

Any electronic structure method requires specifying (a) a representation for the *crystal structure* (and, for random systems such as the PM phases, the way the configurational average is performed), as well as (b) the *type of electronic interactions allowed* by the Hamiltonian and its solver (e.g., forms of exchange and correlation in band theory; dynamic correlation in explicitly correlated theories). In regard to (b), Table I shows the magnetic moments and band gaps calculated by ordinary DFT+*U* for the AFM as well as the assumed ferromagnetic (FM) phases of MnO, FeO, CoO, and NiO. Recall that in the DFT+*U* method[24] as well as related methods such as the self-interaction corrected DFT[29] and the hybrid functionals[30] are all single

particle schemes in which the wave function of the *N* electron system is a single determinant. *We see from Table I that even in the single-determinant DFT+U description with reasonable U=5 eV, which we used across the board for all compounds and spin configurations, these transition-metal monoxides, regardless of the type of magnetic ordering (AFM or FM), exhibit large local moments and band gaps.* This opens the possibility that the actual magnetic order may not be the primary reason for these materials to be insulators, but the existence of on-site magnetic moments caused by breaking of the symmetry between spin up and spin down electronic states may. We will follow this hint by removing in band theory the conceptual and computational barriers to the formation of energy lowering symmetry breaking.

III. Allowing for a polymorphous description of the magnetic structure of the paramagnetic phases : Basic concepts

Gapping in 3D metals can occur due to *magnetic spin effects* even without symmetry breaking (as is the case for the hypothetical FM phase in Table I). In this case there is no atomic symmetry breaking and gapping is a local electronic effect due to the possibility to make majority spin and minority spin occupy different states and render spin up and spin down as closed shells. [Note, however, that the FM phase is not a viable representation for the PM phase that the latter is disordered; also, as Table I shows, E(FM) has a higher total energy than E(PM) even at low temperature]. But gapping in a 3D metal can also occur due to *non-magnetic atom symmetry breaking effects* that can also create close shell structures. This is illustrated by gapping a metal by permitting the geometric flexibility that enables electronic symmetry lowering. For example, the DFT total energy of cubic perovskite $BaBiO_3$ with a single Bi^{4+} site per cell (a metal), is lowered by doubling the cubic perovskite primitive cell, allowing two Bi^{4+} ions to express their multivalent nature by disproportioning into Bi^{3+} + Bi^{5+} (see Ref.[31]) with each site having its own, local bond geometry, a cell-internal symmetry lowering that caused gapping. Similarly (see Ref.[32]) for $CsTlF_3$ being allowed to express the multivalence of Tl in Cs_2 $[Tl^{1+}Tl^{3+}]F_6$ leading to gapping of a previously metallic state. In all such cases, a restricted structural description (one type of octahedron) incorrectly produced a metal, whereas a more flexible description of the cell lowered the total energy and produced the observed insulating gap in band theory. Such geometrical freedom needs to be exercised also for spin alloys to concomitantly examine its effect on the total energy and possible gapping.

Here, we wish to examine if significant on-site magnetic moments might produce a gap also in the PM phases within a single-determinant approach, had these moments not been eliminated at the outset by selecting for the representation for the crystal structure the monomorphous macroscopically averaged configuration $\mathbf{\Sigma}_0$ where each TM site sees the same local environment. In the latter case the global zero moment characteristic of the PM phase is interpreted on an atom by atom basis so $\mu_i(\mathbf{\Sigma}_0) = 0$ at each metal site i, leading in band theory (where large moments mean large exchange splitting) to a band gap $E_g(\mathbf{\Sigma}_0)$=0. The polymorphous approach allows

each TM atom to see a distinct local magnetic environment and a locally varying density-functional potential $V[\rho(\boldsymbol{r}), m(\boldsymbol{r})]$ [where $\rho(\boldsymbol{r})$ and $m(\boldsymbol{r})$ are, respectively, the electron density and magnetization at position $\boldsymbol{r}$] subject to the constraint that the *total* magnetic moment is zero as must be in a paramagnet. We will enquire if such a representation has sufficient geometrical freedom (e.g., unrestricted spatial symmetry) to allow in a self-consistent DFT(+U) calculation the evolution of local magnetic moments on individual sites, if this would lower the total energy. In band theory language, large moments imply large exchange splitting which could enable large gaps.

A. Using the average $\langle \mathbf{P} \rangle$ of the properties $\{\mathbf{p_i}\}$ of individual configurations $\{\boldsymbol{\sigma}_\mathbf{i}\}$ vs. using the property $\mathbf{P}(\boldsymbol{\Sigma}_\mathbf{0})$ of the average configuration $\boldsymbol{\Sigma}_\mathbf{0} = \langle \boldsymbol{\sigma}_\mathbf{i} \rangle$

A common misconstrued approximation in calculating observable macroscopic electronic or magnetic property $\langle P \rangle$ of a disordered random alloy $\mathrm{A}_x\mathrm{B}_{1-x}$ of composition x or of a disordered moment PM phase is to substitute the calculation of the ensemble average $\langle P \rangle$ for property P by the calculation of the property $P(\boldsymbol{\Sigma_0})$ of the *macroscopically averaged configuration* $\boldsymbol{\Sigma_o}$. This monomorphous approximation has been used in the single-site Coherent Potential Approximation (s-CPA) for chemical alloys[33] where all A (B) sites in the random alloy see the same potential V_A (V_B), irrespective of the existence of different local environments for different A sites (characterized by different numbers of A vs. B nearest neighbors to a given central atomic site). This approach in alloy theory forced vanishing charge fluctuations (hence zero Madelung contribution to the total energy[34, 35]) and vanishing atomic displacements,[36, 37 38, 39] both in conflict with more general theories (such as supercells[40],[34, 36, 41] having a polymorphous distribution of different A sites each with its local environment (and same for B sites)

The correct way to calculate the property P of a phase that can have numerous individual configurations $\{\boldsymbol{\sigma}_i^{(n)}\}$ each with property $P(\boldsymbol{\sigma}_i^{(n)})$, (where n is the index of the configuration), is to calculate the polymorphous statistical average $\langle P \rangle = \sum_n c_n P(\boldsymbol{\sigma}_i^{(n)})$ over the ensemble of microscopic spin configurations accessible to the system, instead of assuming $\langle P \rangle = P(\boldsymbol{\Sigma_o})$. The former approach has largely replaced the monomorphous approaches (s-CPA, Virtual Crystal Approximation) in the theory of disordered substitutional alloys $\mathrm{A}_x\mathrm{B}_{1-x}$, producing qualitatively different results[34, 36, 40, 41] in much better agreement with experiment. The same polymorphous approach can be applied to spin disordered phases, i.e the PM phase of Mott insulators.

B. Time average vs. spatial average

In a spin-disordered phase the orientation of the on-site magnetic moments $\boldsymbol{\mu}_\mathbf{i}$ can change over time showing spin wave excitations representing the low energy scale of the

problem; such fluctuations in the *orientation* of the moments have zero overall average. In single impurity DFMT the Hubbard model is mapped onto an equivalent Anderson single impurity model in which the electrons at the impurity interact with a mean field bath those models the rest of the system. There is but a single impurity, which fluctuates in time to give a time average of zero spin.

We examine instead how accurately can one predict the gaps of the PM phases of MnO, FeO, CoO, and NiO within a single-determinant description, for which here we use the DFT+U scheme, if one correctly estimates the statistical average $\langle \mathrm{P} \rangle = \sum_{\mathrm{n}} \mathrm{c_n P}(\boldsymbol{\sigma}_{\mathrm{i}}^{(\mathrm{n})})$ over the ensemble of microscopic spin configurations accessible to the system instead of forcing a zero moment on an atom-by-atom basis. Using a supercell consisting of 2x2x2 or 3x3x3 primitive cells, rather than a single NaCl primitive cell (N=1) permits different local environments to each TM atom. Such a polymorphous representation allows for a number of degrees of freedom, consistent with an overall paramagnetic state, including (i) different number of TM neighbors with spin up and spin down (geometric fluctuations), (ii) different occupations of the 3d orbitals on each TM (occupation number fluctuation), as well as (iii) different local displacements (positional fluctuations), and consequently (iv) different local magnetic moments. The magnitude (zero or otherwise) of these fluctuations is determined in a charge self-consistent DFT calculation by seeking lower total energies. This provides for an intrinsically multi-site representation involving a distribution of transition metals, each with its own local environment. No mean field-embedding bath is needed, and no arbitrarily selected symmetry breaking is involved.

Our underlying conjecture is that time fluctuations that could average the *magnitude* (not *orientation*) of the magnetic moment to zero would involve excitations across the band gap, so the time scale for such fluctuations is slow in relation to the relevant electron energy scale. Thus, the *magnitude* of the on-site moments $|\boldsymbol{\mu}_{\mathrm{i}}|^2$ in gapped PM systems will not be zero, deciding the higher energy scale of the problem. As a result, the time average of the gaps of all configurations could be nonzero. Even though the average $\langle P \rangle \sum_n c_n P\left(\boldsymbol{\sigma}_i^{(n)}\right)$ over the ensemble of microscopic spin configurations is involved, the band gaps and moments $P(\boldsymbol{\sigma}_i^{(n)})$ of individual configurations are nonzero.

Indeed, the fact that the antiferromagnetic ordering disappears at T_N does not mean that the magnetic moments at the transition metal sites go to zero too. On the contrary, the transition metal atoms retain robust local magnetic moments as evidenced by the Curie-Weiss behavior of the magnetic susceptibility as a function of the temperature. This means that the symmetry between spin up and spin down electronic states is instantaneously broken at each site thus allowing the localized magnetic moments to form. In contrast, in the naïve non-magnetic approximation to the PM spin configuration[4, 1717-19] one imposes perfect symmetry between spin-up and spin-down which is the symmetry that one obtains via time averages. However, properties such as band gaps calculated by using this zero average magnetic configuration does not correspond to the property calculated as an average of the properties of the spin configurations

that the system traverses. A possible way to allow for a polymorphous description of the PM phase that permits the development of local moments in a variational calculation is the Special Quasirandom Structure (SQS) construct.

C. The special quasi-random structure (SQS) as a finite supercell realization of a polymorphous paramagnet, not a snapshot configuration

Let us focus on the band gap as the property *P* to be calculated. Instead of calculating the band gap for many snapshot configurations $\{\boldsymbol{\sigma}_i^{(n)}\}$ and averaging the corresponding band gaps $P(\boldsymbol{\sigma}_i^{(n)})$, we construct a single supercell of *N* sites that *approximates the polymorphous configurational average*. This is done by requiring that the pair and multibody atom-atom correlation functions in this special *N* site cell best match the analytically known correlation functions for the infinite, perfectly random configuration.[42, 43] Convergence with respect to *N* must be examined; we use $N \leq 216$ atoms/cell finding that the moments and the total energy have stabilized. The SQS fully complies with the polymorphous description of the PM phases that we want to apply here. An observable P calculated for such a structure is not simply the property of a single snapshot configuration but approximates the ensemble average $\langle P \rangle$ for the random configuration (see Appendix A for the SQS construct[44-46] and the explanation of how an SQS approximates the ensemble average for a random system).

It is clear that describing random alloys by periodic structures will introduce spurious spatial correlations in the moment configuration beyond a certain distance ("periodicity errors"). However, many physical properties of solids are characterized by microscopic length scales that can be ordered according to their typical size so as to establish a hierarchy. For instance, interactions between distant neighbors generally contribute less to the total energy than do interactions between close neighbors. Therefore, the guiding idea in the construction of special quasi-random structures is to obtain within such structures a close reproduction of the perfectly random network for the first few shells around a given site, while the periodicity errors originate from the arrangement of the more distant neighbors. In this respect, the SQS construct is reminiscent of the 'special **k** points' used for Brillouin zone integration[47, 48] in the sense that the selected **k** points are not meant to reproduce properties that reflect mostly the long-range order. The accuracy of the SQS improves as one uses larger SQS cell representation (analogous to using more k points in BZ sampling methods) in which longer range correlation functions can be matched. We have used 64-tom (2x2x2 primitive cells) and 216-atom (3x3x3 primitive cells) SQS's.

The SQS, as we just pointed out, is a convenient computational tool to approximate ensemble averages. It has been shown that relatively small SQS produce numerically the same property values as far larger (ergodic) randomly selected supercells (see Ref.[49]). Note, however, that the SQS approach is not to be confused with the commonly practiced supercell

approach. In the supercell approach, one occupies lattice sites by different spins using, say, a random statistics (i.e., via coin toss) or some choice of short-range order. However, each such occupation pattern corresponds to a single snapshot and in order to calculate the observable property $\langle P \rangle$, which is an ensemble average, one should average the properties $\{P_i\}$ of different supercell snapshots. In the SQS approach the property P_{SQS} calculated for one SQS provides an approximation of the average $\langle P \rangle$ which is progressively improved by increasing the size N of the SQS and by extending the order and size of the figures that the SQS algorithm tries to hierarchically match. Because the SQS is a polymorphous approach, it allows chemically identical sites to develop their own, energy-lowering displacement patterns. In the transition metal monoxides investigated here the minimization of the total energy for the PM phases shows negligible positional atomic displacements relative to the rock salt positions (less than 0.07 A in amplitude. Examples of previous works that use the SQS construct to model magnetic disorder are Ref. [50] and Ref. [51] in which magnetic SQSs were used to model UO_2 and CrN respectively finding encouraging results.

Fig.1 shows the SQS we use for the random PM phase. The histogram in Fig.1 illustrates that, while in the AFM phase (formed by doubling of the primitive rock salt cell) each metal atom has 6 spin-up and 6 spin-down metal neighbors [denoted by (6,6)], in the SQS representation of the high-temperature PM phase there is a *distribution of local environments*, e.g., (4,8), (6,6), (8,4) etc. The landscape of the self-consistent DFT potential $V[\rho(\boldsymbol{r}), m(\boldsymbol{r})]$ corresponding to the SQS, in effect, allows each metal site to experience its own distinct 'particle-in-a-box' type potential, simply because chemically identical metal sites that have different neighbors 'see' different local potentials. Just as the doubling of the primitive cell is needed to produce anti-ferromagnetism in the low temperature AFM phases, the magnetic SQSs allow to capture the different local patterns in the distribution of the magnetic moments that characterize the PM phases. As we will see below, such polarization of the charge density into certain areas of space (not necessarily localization in the sense of 2 electrons on one site as in the Mott-Hubbard picture) is important in driving the selective occupation of certain *d* orbitals out of the originally degenerate ones. The consequence is the development of large energy gaps.

D. Allowing geometrical broken symmetry and occupation broken symmetry

Within the SQS construct we consider four types of fluctuations introduced by broken symmetry (with respect to NaCl with one TM/cell and nonmagnetic):

(a) *Geometric fluctuation*: different local geometrical environments for chemically identical TM atoms in the lattice. Specifically, a different number of spin-up vs spin-down sites can exist around each TM sites see Fig. 1. Here the 12 (next nearest) neighbor TM atoms to a central TM atom can have 6 up spin + 6 down spin, or 4 up +8 down, etc.). This is afforded by

the SQS construct, treating the PM phase as a spin alloy. The system is in PM-phase (total magnetic moment = 0).

(b) *Occupation number fluctuations* whereby atomic sites with partial occupation of initially degenerate levels (e.g., 2 electrons in the threefold degenerate t_2 level) can have different assignments of the electrons to the degenerate partners. Occupation broken symmetry means that for every cobalt atom, the occupations on different d-states are always integer [such as (1,0,1) in 2 electron t_2 , or (1,0) in single electron e level, rather than using fractional and equal occupation such as (2/3,2/3,2/3) in the t^2 case, or (1/2,1/2) in the e^1 case.

In a charge self-consistent DFT calculation, the fluctuations (a) and (b) could lead also to further energy lowering via

(c) Site-to-site local magnetic moment fluctuations, and

(d) Displacement fluctuations (i.e, atomic relaxation).

The key point is that the polymorphous approach used here all such symmetry breaking mechanisms— geometric [(a) and (d)] or non geometric [(b) and (c)] are considered simultaneously as long as they lower the energy.

On the technical side, we note that to ensure that the occupation pattern does not correspond to a local minimum, one initially applies a 'nudge' in the occupation matrix (see Refs.[50, 52-54]) and then proceeds with the charge self consistent DFT calculation. Appendix B describes the protocol used for nudging the site occupations and site relaxations.

E. The role of *U* in DFT+*U*

To treat open shell systems with degenerate orbitals (such as 1 or 2 electrons in a triply degenerate t_2 level) one requires in DFT an exchange correlation (XC) functional that distinguishes occupied from unoccupied orbitals (so 1 or 2 of the degenerate t_2 partners will be occupied by integer electron(s) and the other will be kept empty, rather than occupying all partners by fractional electrons). This requirement means that the XC functional contain an exchange correlation derivative discontinuity, i.e that the functional should belong to rung 4 or 5 of the DFT hierarchy: Meta-GGAs (like SCAN) are "semilocal" functionals of the non-interacting density matrix, and belong to Rung 3. In contrast, DFT+U, Hybrid functionals and self interaction corrected (SIC) functionals are all nonlocal functionals of the non-interacting density matrix and they are classified as Rung 4. RPA, which is a nonlocal functional of *all* occupied and occupied orbitals and their orbital energies, belongs to Rung 5. *The derivative discontinuity of the exchange correlation energy is missing in the first three rung of DFT functionals, but present in the 4th and 5th rungs.*

We use here the simplest nonlocal XC ie DFT+U, a method can be seen as an approximation to the more rigorous self- interaction correction. We used the PBE+U nonlocal approximation to the exchange and correlation functional; for simplicity, we use a constant value of $U - J = 5.0$ eV (the parameter in the DFT+U formulation of Ref.[55]) for all materials in this study, although, most likely one can improve agreement with experiment by tweaking U separately for each

compound. In the DFT+U method the DFT total-energy functional is corrected by two terms (Refs.[20-24, 55-59]). The first term is a mean-field approximation of the electron-electron interaction within a subset of localized orbitals (here, the d orbitals). The second term subtracts the contribution of the electron-electron interaction already accounted for in the approximate functional and largely consists of the self-Coulomb interaction (a manifested one body effect)..

Despite the impression suggested by the letter (Hubbard) "*U*", the DFT+*U* method (perhaps better renamed DFT+*V* to avoid such a confusion) does not imply correlation *in the Hubbard Hamiltonian sense*. We note that the numerous practitioners apply these methods with the belief that they model many-body correlations. DFT+*U*, as well as the hybrid functionals and SIC DFT, are all methods in which the wavefunction of the N electron system is a single determinant. In single-determinant, band structure approaches each band structure calculation occupies its levels in a single specific manner by electrons (a single Slater determinant) and different possible patterns of occupation of levels by electrons (which can be built in separate band structure calculations) have no way of seeing each other.

F. The role of spin disorder vs spin order

We note from Table I that the FM spin arrangement is monomorphous and has a gap due to its long-range order, but it's obviously not a good model for the paramagnetic phase that is magnetically disordered. In a disordered phase we allow for identical atoms to have the opportunity to experience different local structural environments. The exchange and crystal field interactions present in DFT SQS are local effects that do not need a long-range magnetic ordering to mix and split the d levels, and as such these local effects drive the opening of a gap in the overall magnetically disordered phase. Furthermore, the SQS PM phase has lower energy than the FM phase by 59.5, 45.1, 67.6 and 79.0 meV/formula unit for NiO, MnO, FeO and CoO, respectively (See Table I) so the FM description is not selected.

Table I shows that the internal energy at T=0 of the spin disordered PM phase is higher than that of the AFM phase at T=0, as expected. We clarify that for the spin disorder PM phase the free energy is F=E-TS where S in entropy, so at T=0 the AFM phase is lower in energy, and as T grows the free energy of the PM phase E-TS is lowered until it becomes the lowest energy phase. However, we do not aim to calculate the Neel temperature. Such calculations within DFT are known in the literature (e.g Franceschetti *et al.*, Ref.[60] and Daene *et al.* , Ref.[61]).

IV. Summary of the main results on the PM phases.

Before we discuss the physical picture that emerges we state the results obtained for the magnetically ordered AFM and FM phases and for the magnetically disordered PM phases, which we modeled by a polymorphous description. As we are not interested here in fitting the calculated gaps and moments to experiment, for simplicity we use DFT+*U* with a generic constant *U*= 5 eV same for the FM, AFM, and PM phases and all compounds; we also assume collinear moments and neglect short-range order in the PM phase

assuming perfect randomness (the high temperature limit). In this paper we do not compute transition (Neel or Curie) temperatures but focus on the minimal physics needed to get gapping and moments in such Mott insulators. Examples of calculated transition temperatures from DFT inputs are given, for example, in Ref [60]. All such fine-tuning corrections can be used in the future if one seeks more accurate, material-dependent physics. The schematic of Fig. 2 summarizes the hierarchy of site-specific effects that remove the degeneracy in the four monoxides. The calculated values of moments, total energies and band gaps are listed in Table I and reported in the projected density of state plots of Figs. 3 and 4. The key ingredient of the theory is allowing for chemically identical sites to develop their own unique local environments and potentials rather than forcing a monomorphous representation which leads in the PM phase to non-magnetic unit cells. *We see from Fig 3 and 4 and Table I that a straightforward band structure description with appropriate structural/configurational input and reasonable value of the self-Coulomb U parameter captures the moment formation and gapping in the AFM as well as PM phases of the classic Mott insulators.*

V. Analysis of the results

A. Analysis of the occupations of the localized orbitals

For our analysis of the DFT+U results we sought linear combinations of the *d* orbitals that form a good representation of the point-group symmetry at the TM sites. The *d*-orbital occupation matrix that enters the "+*U*" term of the DFT+U energy functional is calculated using the t_{2g} and e_g orbitals as basis. However, the actual magneto-crystalline order in the AFM phases, or the lack of it in the PM phases, breaks the cubic point-group symmetry at the TM sites. In such a case a good representation for the *d* orbitals, which is often referred to as the "crystal field representation", is that defined by the eigenvectors of the occupations matrices. This representation is also meaningful in terms of the mechanism that drives the band gap opening. The sum of the probability distributions of the eigenvector functions with spin down each weighted by its occupation gives the distribution of the minority-spin electrons density around the transition metal sites, which we inspect in the following. See Appendix B.1 for more details on this representation.

B. Making sure that the electronic structure DFT description does not get trapped in a high symmetry basin.

On the technical side, one needs to assure that the self-consistency cycle is conducted so as to avoid that it get trapped in a high-symmetry solution but to permit the

exploration of broader positional as well as wave function symmetries. In the case of systems in which the crystal field produces degenerate states that are partially filled, one must explore lowered symmetries of the electronic state by allowing for distortions of the lattice.[23, 24, 62] Thus, we permit an initial 'nudging' of the atoms off the high symmetry sites (and see if the quantum mechanical forces tend to restore such high symmetry positions or prefer Jahn-Teller-like displacements). At the same time, one needs to assure that the electronic self-consistency cycle could explore a broader range of wave function symmetries without getting trapped in high-symmetry solutions. To this end we avoid charge density symmetrization during the electronic self-consistent iterations. In the case of the PM phases, we "nudge" the systems initially with unequal *d* orbital occupations. See Appendix B.2 for the details of the nudging protocol. Starting from such an orbital configuration helps the self-consistent solver to converge towards a solution in which the *d* orbitals mix to form linear combinations whose occupations ultimately are either close to one or zero.

VI. Results: The magnetically ordered AFM phases

The AFM phases of MnO, FeO, CoO, and NiO have been studied by DFT[64, 65] as well as its extensions and corrections, including DFT+U,[23, 62] hybrid functionals,[66] and SIC.[67] Here we briefly describe our results of the evolution of the band gaps (Fig. 2) and provide the density of states [Fig 3(a,b) and Fig 4(a,b)] to establish a common basis for discussing later the generalized supercells needed to capture the physics of the PM phases. As shown in Fig. 2, in the ideal cubic rock salt structure ($Fm\bar{3}m$ space-group) the crystal field splits the atomic *d* levels into spin-up and spin-down t_{2g} and e_g levels. The AFM-II magnetic ordering already breaks the cubic space-group magneto-crystalline symmetry even without distortions to the ideal cubic lattice. The lattice relaxations that are experimentally observed in the low-temperature phases of these monoxides[68-70], lower the point-group symmetry of the crystal field at the TM sites with respect to that of the ideal cubic structure. See Appendix C for the details of the relaxed crystal structure of the AFM phases that we obtained by our DFT+*U* calculations. Qualitatively, a similar combined effect of the exchange and crystal field interaction is the mechanism that drives the gap opening in the PM phases and provides a unifying, single-particle description of the insulating character of both the magnetically ordered and magnetically disordered phases. We, therefore, illustrate this mechanism starting with the AFM phases, as well as the hypothetical FM phases, through the same protocol used for the PM phases.

A. AFM MnO and NiO.

AFM MnO and NiO exhibit a $R\bar{3}m$ magneto-crystalline structure in which the TM crystal field has the rhombohedral D_{3d} point-group symmetry. A crystal field of this symmetry

mixes the t_{2g} orbitals so as to give the a_{1g} singlet and the e_g' doublet (Fig. 2(c)). The e_g orbitals are symmetry invariant to the D_{3d} symmetry operations and are often indicated as e_g''. Figures 3(a)-(b) depict the DOS of MnO and NiO projected onto the cubic t_{2g} and e_g orbitals. In MnO, the Mn^{2+} ions exhibit the d^5 electronic configuration which results into the five spin-up $d^{\uparrow}$orbitals fully occupied. A band gap opens in MnO between the fully occupied spin-up $d^{\uparrow}$ orbitals and the empty spin-down $d^{\downarrow}$ orbitals. In NiO, the Ni^{2+} ions exhibit the d^8 configuration which corresponds to the five spin-up $d^{\uparrow}$orbitals fully occupied and the $t_{2g}^{\downarrow}$-derived orbitals also fully occupied. A band gap opens in NiO between the occupied $t_{2g}^{\downarrow}$-derived levels and the empty $e_g^{\downarrow}$-derived levels.

B. AFM FeO and CoO.

Fe^{2+} and Co^{2+} in FeO and CoO are, respectively, in the d^6 (meaning one electron in the spin-down d states) and d^7 (meaning two electrons in the spin-down d states) configurations. Our DFT+U calculations, in line with earlier studies[23, 24, 62], show that a gap opens in FeO and CoO already in the undistorted cubic lattice because of the symmetry lowering induced by the AFM-II ordering. FeO opens a gap by occupying the $a_{1g}^{\downarrow}$ singlet while the $e_g'^{\downarrow}$ doublet is in the conduction. The opposite occurs in CoO with $e_g'^{\downarrow}$doublet occupied by two electrons while the $a_{1g}^{\downarrow}$ singlet is in the conduction. FeO[71] and CoO[69, 70] lower their total energies with respect to the ideal cubic lattice through tetragonal distortions of the metal-oxygen coordination octahedra that are accommodated within a monoclinic cell with C2/m space group symmetry (see Fig. A1 and Table. A1 in Appendix A) for a description of the calculated equilibrium crystal structure). In FeO there is a compression of the in-plane bonds and an expansion of the out-of-plane ones, while the opposite occurs in CoO. Figures 4(a)-(b) depict the DOS of monoclinic FeO and CoO projected onto the cubic t_{2g} and e_g orbitals: FeO and CoO continue to be insulating in the stable AFM monoclinic phase as in the higher-energy, AFM undistorted cubic phase. The orbital mixing that occurs because of the tetragonal distortion of the coordination octahedra is reflected by the shape of the spin-down electron density $\rho^{\downarrow}(\boldsymbol{r})$. In FeO, $\rho^{\downarrow}(\boldsymbol{r})$ has a square-planar shape rotated by 45° degrees around the z axis (see Fig 5(a)). In CoO, $\rho^{\downarrow}(\boldsymbol{r})$ has an octahedral shape with the vertical axis lying along the diagonal of the x-y plane (see Fig 5(b)). A detailed analysis of $\rho^{\downarrow}(\boldsymbol{r})$ in terms of the orbital mixing obtained in the DFT+U solution is performed in Appendix D.1.

VII. Results: The magnetically disordered paramagnetic phases

The DFT+U calculations of the PM phases of the four monoxides modeled with the magnetic SQS produce insulating solutions with strong magnetic moments at the TM sites (see. Table I for the gaps and magnetic moments at the transition metal sites obtained in these SQS calculations). The minimization of the total energy for the PM

phases of NiO, MnO and FeO, modeled by the SQS shows negligible positional atomic displacements relative to the rock salt positions, thus, no significant broadening of Bragg diffraction peaks is expected. The projected DOS (PDOS) on the metal *d* orbitals are depicted in Fig. 3(c,d) for MnO and NiO and Fig. 4(c,d) for FeO and CoO. For the sake of comparing the PDOSs across the whole series of oxides and magnetic phases included in this study, we project the DFT+U wave functions on t_{2g} and e_g orbitals. However, in the polymorphous description which is implemented through the magnetic SQSs, the crystal field at each TM site shows a low point-group symmetry which in turn allows for the t_{2g} orbitals to mix among themselves and possibly also with the e_g orbitals. The magnetic disordered phases of MnO and NiO exhibit gaps that in both cases, as can be seen from the PDOSs in Fig 3(c,d), open between sub-bands that derive predominantly from the t_{2g} and e_g orbitals and are both filled in a similar fashion as in the magnetically ordered AFM phases.

The PDOS plots of FeO and CoO in Fig. 4(c) and 4(d), respectively, show that the gap originates in both systems mainly from a splitting in the t_{2g}-derived states. An inspection of the density $\rho^{\downarrow}(\boldsymbol{r})$ of spin-down electrons of PM FeO and CoO (see Fig. 6(a,b)) and of the eigenvectors of the occupation matrices calculated at the TM sites (see Appendix D.2) shows that the gap is the result of the mixing of the *d* orbitals in the low-symmetry crystal field that characterizes each site in the disordered phases and of the splitting of these mixed orbitals that lifts the degeneracy of the unperturbed d states. In PM FeO, $\rho^{\downarrow}(\boldsymbol{r})$ at the Fe sites (Fig 6(a)) has a square-planar shape lying on one of the Cartesian planes and it is not tilted by 45^0 around a Cartesian axis as in AFM FeO (see Fig. 5(a) and 5(c) for a comparison between $\rho^{\downarrow}(\boldsymbol{r})$ in AFM FeO and PM FeO), with the specific plane varying randomly from site to site. Sites 4 and 14 in Fig. 6(a) are examples of two distinct orientations of $\rho^{\downarrow}(\boldsymbol{r})$ around the Fe sites in PM FeO. The analysis of the eigenvectors of the occupation matrices in Appendix D.2 shows that this square planar shape originate from one t_{2g} orbital almost completely filled.

In PM CoO, we observe (see Fig. 6(b)) that $\rho^{\downarrow}(\boldsymbol{r})$ shows two types of shapes at the Co sites: a cylinder-like shape (e. g., at site 14 in Fig. 6(b)) aligned to one of the Cartesian axes, and an octahedron-like shape (e.g., at site 4 in Fig. 6(b)), with the apex of the octahedron that, as opposed to the similar octahedral shape that $\rho^{\downarrow}(\boldsymbol{r})$ displays in AFM CoO, is tilted away from the Cartesian planes and points into a direction that varies randomly from site to site. Figs. 5(b) and 5(d) display $\rho^{\downarrow}(\boldsymbol{r})$ at the Co sites in AFM CoO and PM CoO respectively and show the different orientation of the octahedral shape in the two cases. From an inspection of the eigenvalues of the occupation matrices at the Co sites within the SQS (see Appendix D.2) we observe that at each site two eigenvectors $\phi_{Co}^{(1)}$ and $\phi_{Co}^{(2)}$ have occupations of ~0.9, that is, are almost completely full and provide the dominant contribution to $\rho^{\downarrow}(\boldsymbol{r})$ at the Co sites. The two different types of the shape of $\rho^{\downarrow}(\boldsymbol{r})$, found for example at site 4 and 14 in Fig. 6(b), originate

from two distinct modes of mixing of the *d* orbitals to which correspond two distinct pairs of (nearly fully) occupied eigenvectors $\left\{\phi_{Co}^{(1)}, \phi_{Co}^{(2)}\right\}$. At the sites where $\rho^{\downarrow}(\boldsymbol{r})$ shows a cylindrical shape (e.g., site 14 in Fig. 6(b)) the eigenvectors $\left\{\phi_{Co}^{(1)}, \phi_{Co}^{(2)}\right\}$ are two of the three t_{2g} orbitals. At sites where $\rho^{\downarrow}(\boldsymbol{r})$ shows a tilted octahedral shape, the eigenvectors $\left\{\phi_{Co}^{(1)}, \phi_{Co}^{(2)}\right\}$ are normalized linear combinations of the three t_{2g} orbitals with contributions also from the e_g orbitals. Analytic models of the probability densities $\left|\phi_{Co}^{(1)}\right|^2$ and $\left|\phi_{Co}^{(2)}\right|^2$ and of their sum $\left|\phi_{Co}^{(1)}\right|^2 + \left|\phi_{Co}^{(2)}\right|^2$ are displayed in Fig. A3 in the Appendices; these models are consistent with the tilted octahedral and the cylindrical shape of $\rho^{\downarrow}(\boldsymbol{r})$ at the Co sites in PM CoO obtained in the DFT+U solution.

The modality of orbital mixing and level splitting revealed by the present calculations are analogous in the AFM and PM phase of the respective oxides. This helps explains the fact that the magnetic moments in the SQS PM configurations converge to values whose average is within to less than 1 % of the AFM values (Table I). At the same time, the magnetic disorder decreases the band gap of MnO, NiO, and CoO with respect to the value in the AFM phase.

VIII. Discussion

A. The physical picture of gapping of the PM phase: The role of different symmetry- breaking modes in the PM phase

We considered the following degrees of freedom that induce the symmetry breaking with respect to nonmagnetic NaCl-structure with one TM per primitive cell: (a) geometric symmetry breaking via the local environment distribution supplied by SQS; (b) occupation number broken symmetry (OBS); (c) displacement fluctuations (i.e., atomic relaxation), and (d) site-to-site local magnetic moment fluctuations. In CoO, we illustrate the effects of these fundamental fluctuations in Fig. 7 by starting from the most complete calculation ("Level IV" below) and 'peeling of the onion' (i.e., removing the effects one by one), inspecting total energies, band gaps, local moments and atomic displacements for the following 4 levels:

Level IV theory: SQS + OBS, with relaxation; allows effects (a), (b), (c) and (d). Fig 7(a) shows the projected density of states as well as total energy, band gap and average cobalt local magnetic moment for level IV of the 216-atom rock salt CoO supercell. It represents a very large energy lowering of -2219 meV/formula units relative to the monomorphous non magnetic description (level I below) and yields a band gap of 2.39 eV and local moment of 2.75 BM. Some of its properties include:

(i) Although the $\mathrm{t_g}$ and $\mathrm{e_g}$ representations are mixed by the various symmetry breaking channels, one can observe that the hole is localized predominantly on $\mathrm{t_{g\downarrow}}$ derived state rather than

e_g state: The occupation broken symmetry is manifested by the fact that 2 electrons occupying the T_1, T_2 and T_3 components in the spin down t_g band causes the band to split into the fully occupied (by 2 electrons) VBM and an empty t_g (CBM) derived spin down conduction band. Together with the 3 electrons in the deeper spin up t_g band and 2 electrons in the spin up t_g band, leads to the $t_+^3\, e_+^2\, t_-^2$ configuration akin to the $^3T_1$ multiplet (spin 3/2) where the hole is distributed in the t_g-like band. Placing instead the hole in the e_g-like band leads to a higher energy ^2E multiplet.

(ii) *The atomic displacements are configuration-dependent and average to small amplitudes:* Relaxation causes small atomic displacements, with displacement directions depending on the configuration selected, so the orientation average of the displacements if far smaller than in any particular configurations. On average, oxygen atoms have larger displacements than cobalt -- the maximum displacement on oxygen is 0.147 Å, while the maximum displacement on cobalt is 0.073 Å.

(iii) *The band edges do not look like upper and lower Hubbard states but are oxygen derived:* The orbital make up of the band edges (Table II(a) and Fig 7(a)) shows that the VBM is made predominantly of oxygen *p* orbitals (down-spin VBM) and roughly equal amounts of oxygen and cobalt *d* (up-spin VBM) whereas the lowest CBM is predominantly oxygen *p* with some cobalt *d* hybridization. Thus CoO (as well as the other oxides discussed here with late transition metal cations having rather deep 3*d* orbitals) does not have the proverbial lower Hubbard *d* VBM and upper Hubbard *d* CBM, but are in fact charge transfer type band edges more similar to ordinary semiconductors such as ZnO rather than to early transition metal oxides (of V and Ti) that have more significant d character in at least one of the two band edges.

Level III theory: SQS + OBS but no relaxation; allows effects (a), (b) and (d). This level is the same as level IV but no sublattice relaxation. Fig. 7(b) shows the density of states and provides the total energy and other characteristics. The effect of atomic displacements is small. The total energy of relaxed system is 9.5 meV/atom lower than the unrelaxed one, and the orbital make up of the band edges (Table II(b)) is rather unchanged. By comparing the occupation matrices we also find that in the unrelaxed solution the e_g states do not mix with the t_g states e.g the spin down valence states are a superposition of the type, e.g., (dxy, dyz). After relaxation the valence band remained basically pure t_g with little contamination from the e_g states.

Level II theory: SQS, no OBS (freezing equivalent occupation on each t-like state), no relaxation; allows effects (a) and (d). This level of theory includes different local environments (via SQS) in the 216-atom rock salt CoO supercell, but forces equal occupation of the members of a degenerate t_g -like spin down state with components T_1, T_2 and T_3, i.e., instead of placing two electrons in two of the partners and zero in the third, this central field like approximation places (2/3, 2/3, 2/3) electrons in each partner. This places the Fermi level inside the down-spin t_g band leading to a metal. Fig 7(c) shows the density of states and total energy revealing a dramatic increase (494 meV/f.u.) in total energy relative to Level III, just 1706

meV/formula unit below the level I. Despite the gap being zero, this approximation gives a non-zero local magnetic moment.

Level I theory: no SQS (non-magnetic monomorphous description), no OBS, no relaxation; allows no symmetry breaking effects. At this lowest level often used in the past as the DFT rendering of paramagnets involves a primitive NaCl-structure unit cell (1 Co + 1 O). There is no spin-polarization, so the two spin channels (with plus and minus values) are exactly the same. The total energy is very high relative all other theoretical levels; the band gap and moments vanish, and the Fermi energy lies in an e_g-like band instead of the correct t_g-like band as in the other levels of theory.

B. The existence of many broken symmetry configurations in the PM phase

Each independent broken symmetry configuration corresponding to a choice of occupation patters can have, in principle different charge density, total energy, local moments, and band gaps. The ultimate solution for the PM phase should correspond to a symmetrized combination of these configurations. Indeed, as explained in Sec. III. A above, the correct way to calculate the property P of a phase that can have numerous individual configurations $\{\boldsymbol{\sigma}^{(n)}\}$ each with property $P(\boldsymbol{\sigma}_i^{n)})$, is to calculate the polymorphous statistical average $\langle P\rangle = \sum_n c_n P(\boldsymbol{\sigma}^{(n)})$ over the ensemble of microscopic configurations. In general, the combination needs to be symmetrized, and if many-body configuration interaction is to be considered the problem needs to be subjected to this additional diagonalization step. Table III illustrates different configurations for the 216 atom SQS of the PM phase of CoO (Level III). We see that each of these configurations are closed shell and have rather similarly large band gaps and moments. *According to our basic conjecture discussed in Sec. III.B we expect that the symmetrized superposition state will also have the similarly large gaps and moments, ie that the interaction between these base configurations will be weak.* The single determinant band approach used here neglects such dynamic interaction between configurations and would fail when the neglected interaction is strong. This is not the case in the currently considered compounds that are closed shell (level IV or III) with large band gaps and are thus expected to be well represented by single determinant approach.

C. Mott localization and double occupation is not involved in the present physical picture

The bands obtained in the current single determinant mean field band structure theory are conventional single-particle states and should not be confused with the lower and upper Hubbard bands[72, 73] that characterize the solutions of the Hubbard model. The Mott mechanism requires that the electrons move across the lattice forming states on certain

atomic sites with doubly occupied *d* orbitals and empty *d* orbitals on other sites (i.e,, not a Bloch Periodic band structure picture) while the overall charge number is conserved. These types of excited configurations correspond respectively to the upper and lower Hubbard bands, which are truly "dynamic" charge bands and correspond to many-body configurations, whereas the present approach produces gapping without such a mechanism, different than the Mott gap opening mechanism described in the textbooks. That it is not entirely surprising that d electron strong correlation is not the deciding factor for these binary oxide systems as can be gleaned from Fig 7 and Table II showing that the valence band and conduction band edges consist of oxygen p and transition metal s orbitals, not the proverbial d-like lower and upper Hubbard bands.

E. Comparison with other approaches

Previously the paramagnetic phases, including those of the present TM oxides, have been modeled by the disordered local moments (DLMs)[74-76] approach which has been implemented within the single-site coherent-potential approximation (CPA).[11, 33, 61, 77] This approach assumes that the Schrodinger equation potential seen by chemically equivalent atoms in the disordered PM phase are all equal even though such atoms have distinctly different local environments (such as number of neighbors with spin up vs. spin down, see Fig. 1). This picture automatically ignores the existence of inhomogeneous distribution of moments and charges. This is valid only when the local environment flips its spin so fast that a central atom does not distinguish if its environment is made of up spins or down spins but all can be described as some average. This is unlikely to be the case in insulators (such as Mott insulators) where the screening is ineffective. This DLM view leads to equal local moments on all TM atoms irrespective of their environments. The DLM approach is virtually equivalent to the so-called "Hubbard III" approximation[14] in regard to the treatment of the spin disorder. DLM and Hubbard III are in turn related to the DMFT approach, with the difference that DLM and Hubbard III are unable to describe quantum fluctuations which are instead described by DMFT[16]. Similarly, to the DLM description, DMFT is inherently a single-site theory in which all sites of a given species (e.g., all the Co sites in paramagnetic CoO) are geometrically equivalent.

The Special Quasi-Random Structure construct is an effective way to establish a physically grounded representation of the random magnetic configuration for three reasons. First, an SQS is constructed so that a property calculated using it is a close estimate of the ensemble statistical average that would be required to calculate that property for a fully disordered phase. Therefore, using one SQS one can obtain reliable estimates of ensemble averages, i.e., the relevant quantities for the paramagnetic phases, by calculating one configuration instead of many randomly-generated configurations. Second, an SQS allows for a variety of local magnetic environments and for multiple patterns of uneven *d* orbital occupations that both concur to breaking the cubic symmetry and fully lifting the degeneracy of the *d* orbitals. Finally, it is straightforward to construct SQS that represent the property of imperfectly-random ensembles, i.e., those that have short range order (SRO) and are thus better

representative of PM phases closer to the Néel temperature. Instead of constructing the SQS by fitting to the analytically known random pair and many body correlation functions (see Appendix A), one can fit to independently measures or calculated correlation functions that incorporate SRO.[78]

In conclusion, in the present study we find that the DFT+U method, which is a generalized Kohn-Sham approach reproduces the insulating character and on-site magnetic moments of the prototypical Mott insulators MnO, NiO, CoO, and FeO when applied to SQSs, which approximate closely the ensemble average over the random magnetic configurations.

Appendix

For AFM phases we use low temperature lattice vector symmetry. Even in NiO and MnO the spin symmetry alone changes the space group from NaCl to Rhombohedral R3-m [because we selected (111) type AFM]. For FeO and CoO the lowest energy AFM cell symmetry is monoclinic C2/m. We then optimize the structure to achieve very small quantum mechanical forces. Note that the AFM structure can be Jahn Teller distorted (FeO, CoO, see Fig. 2)

For PM phases we use the supercell shape as the macroscopically observed high T cubic lattice vectors, keeping only the cell-internal atomic positions as variables during force calculations.

In practice this can be done in steps such as (i) Freeze one choice at the time of OBS, and a frozen cell-internal atomic geometry, and run charge self-consistency. Do a few OBS choices independently, called ``configuration i"; (ii) Unfreeze the OBS choice starting from (i), while the geometry is still unrelaxed, and perform charge self-consistency.

(iii) Unfreeze the previously unrelaxed geometry, seeking a minimum. In practice, to avoid local minima, this requires an initial nudge in the form of small random atomic displacements, then following the calculated forces to geometries with vanishing forces.

Another protocol involves performing atomic relaxation concomitantly with steps (i) and (ii). Here in step (i') one freezes a given choice of OBS, and performs a charge self-consistent calculation on that frozen OBS while at the same time relaxing the cell internal atomic positions. Do a few OBS choices independently called "configuration i" :(ii') Unfreeze OBS starting from (i'), while the geometry is being re-optimized and do charge self-consistency. In the present case both protocols (i) +(ii) or (i') +(ii') lead to virtually identical results.

Acknowledgements

The work of A. Z. was supported by Department of Energy, Office of Science, Basic Energy Science, MSE division under Grant No. DE-FG02-13ER46959 to CU Boulder. He would like to thank Chris Marianetti, David Singh, Sohrab Ismail Beigi, Gabi Kotliar, George Sawarzky, Igor Mazin, and Olle Helleman for very interesting and extremely useful discussions. G. T. would like to thank also Prof. J. Ketterson of Northwestern University for useful discussions. The crystal structure figures displayed in this article

were generated using the software VESTA.[79] In this research, G.T. used resources of the National Energy Research Scientific Computing Center (NERSC), a U.S. Department of Energy Office of Science User Facility, supported by the Office of Science of the U.S. Department of Energy under Contract No. DE-AC02-05CH11231.

		$R\bar{3}m$				C2/m			
		MnO		NiO		FeO		CoO	
		Exp.	DFT+U	Exp.	DFT+U	Exp.	DFT+U	Exp.	DFT+U
AFM	μ (μ_B)	4.58	4.64	1.9	1.68	4.0	3.71	3.8-3.98	2.72
	E_{gap} (eV)	3.5	1.88	3.5	3.00	2.1	1.66	2.8	2.63
FM	μ (μ_B)	-	4.68	-	1.75	-	3.76	-	2.78
	E_{gap} (eV)	-	0.82	-	2.56	-	1.36	-	2.06
	E_{tot} -E_{tot}[AFM] (eV/fu)	-	0.059	-	0.121	-	0.102	-	0.196
PM	μ (μ_B)	-	4.65	-	1.70	-	3.73	-	2.75
	E_{gap} (eV)	3.7	1.22	4.1	2.16	2.5	1.70	2.4	2.25
	E_{tot} -E_{tot}[AFM] (eV/fu)	-	0.014	-	0.061	-	0.035	-	0.117

Table I: Experimental and DFT+U calculated band gaps E_{gap} and magnetic moments of the transition metal atoms of MnO, NiO, FeO, and CoO in the following phases: (i) AFM with rhombohedral $R\bar{3}m$ space-group symmetry for MnO and NiO and monoclinic $C2/m$ space-group symmetry for FeO and CoO), (ii) FM with cubic symmetry calculated using the same volume per formula unit that was found by total energy optimization for the AFM phase, and (iii) the gap of the PM phases was calculated by a cubic 64-atom $2 \times 2 \times 2$ SQS whose lattice parameter was fixed and the internal coordinates were allowed to relax. The total energies of the PM phases were calculated using a cubic 216-atom SQS in which the lattice parameter was fixed and the atom was kept at the ideal rocksalt positions. In both sets of SQS calculations, the volume per formula unit was equal to the optimal volume per formula unit obtained for the AFM phase. The following are the sources for the experimental values: Ref.[10] for the band gaps of the AFM phases; Ref.[11] for the band gaps of the PM phases; Ref.[12] for the magnetic moments in the AFM phases. We were unable to find in the literature the experimental values of the magnetic moments of the PM phases.

		up-spin VBM	down-spin VBM	up-spin CBM	down-spin CBM
(a) CoO level IV	Energy (eV) (E_{Fermi} = 0)	-0.022	-0.022	2.367	2.453
	Co *s*	0.64%	0.31%	9.00%	0.41%
	Co *d* e_g	52.12%	4.47%	2.80%	2.41%
	Co *d* t_g	1.96%	25.63%	20.78%	95.14%
	O *p*	45.28%	69.59%	67.44%	2.04%
		up-spin VBM	down-spin VBM	up-spin CBM	down-spin CBM
(b) CoO level III	Energy (eV) (E_{Fermi} = 0)	-0.022	-0.022	2.220	2.393
	Co *s*	0.74%	0.32%	6.66%	0.31%
	Co *d* e_g	51.68%	4.96%	1.94%	1.50%
	Co *d* t_g	1.93%	24.92%	23.86%	96.15%
	O *p*	45.65%	69.80%	67.55%	2.04%

Table II: Energies (in eV) and orbital make ups of band edges from DFT+*U* (*U*=5 eV) calculations for (a) level IV (SQS + OBS with atomic relaxations) and (b) level III (SQS + OBS but no atomic relaxations) using the 216-atom rock salt CoO supercell. Level IV started initially from level III calculation. The occupation configuration given by level III in this table is also shown as pattern 1 in Table III.

d Occupation pattern	E_{tot} (eV/f.u.)	E_{gap} (eV)	(μ (μ_B))
1	-11.561	2.26	2.75
2	-11.560	2.37	2.75
3	-11.559	2.26	2.75
4	-11.560	2.35	2.75

Table III: Comparision of the properties of 4 different configurations of SQS-PM CoO obtained by different initial occupation broken symmetries. All are closed shell. Shown are the total energies (in eV per formula unit), band gap (in eV), and average magnetic moment (in Bohr magnetons) at the transition-metal sites. Table A3 in Appendix also illustrates some typical output configurations.

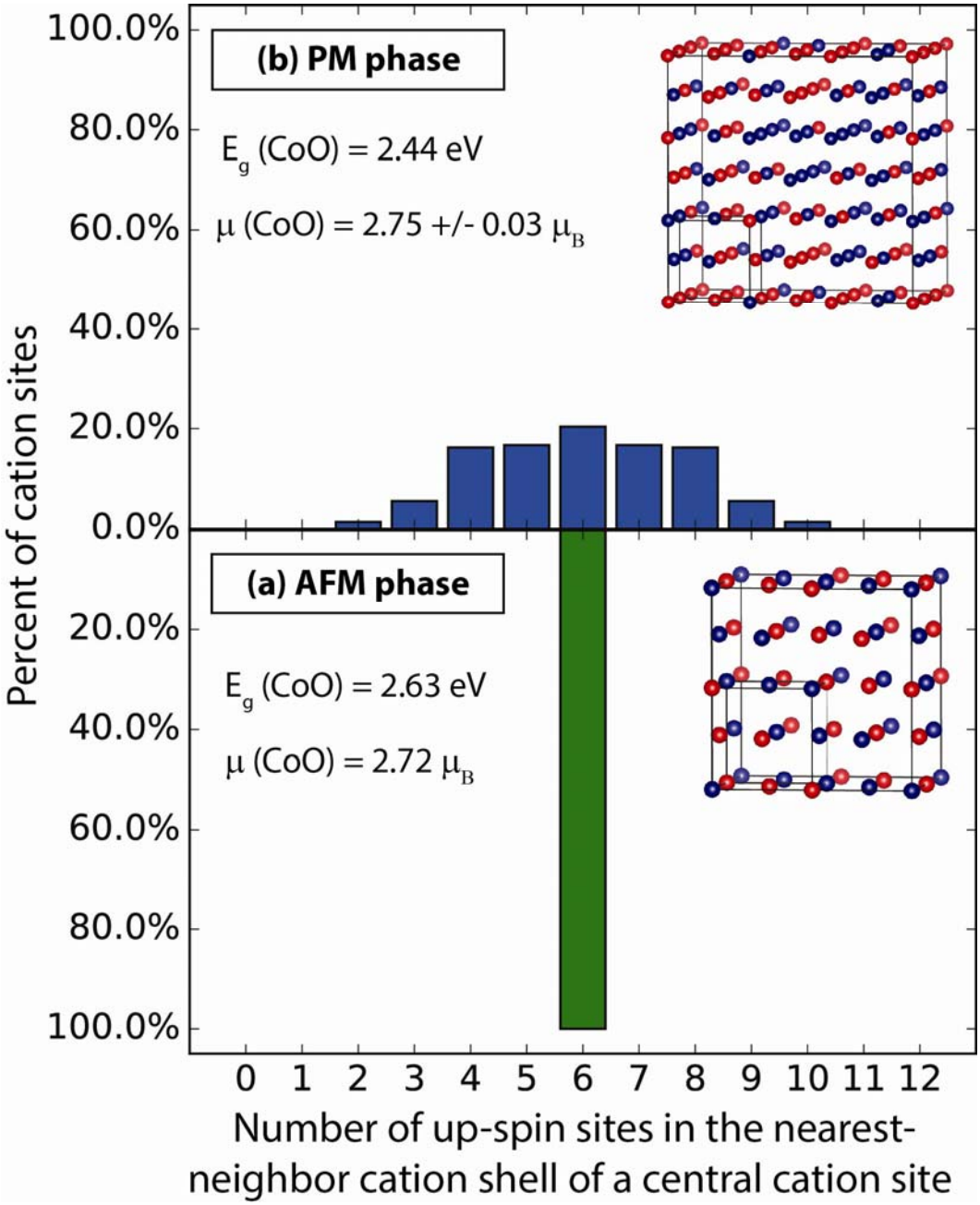

Figure 1. Percent fraction $F(n_{NN}^{\uparrow})$ of cation sites as a function of the number $n_{NN}^{\uparrow}$ of spin-up nearest-neighbor (NN) metal site of a central cation site in (a) the AFM-II phase and (b) the PM phase modeled here by the 216-atom rock-salt SQS shown in the insert (in this model only the metal sub-lattice of the underlying rock salt structure is shown). In the AFM phase $n_{NN}^{\uparrow}$= 6 for all cations while in the PM phase $n_{NN}^{\uparrow}$ varies between 0 and 12 and $F(n_{NN}^{\uparrow})$ approximates a binomial distribution. The frequency of local environment types $F(n_{NN}^{\uparrow})$ was calculated

averaging over a 216-atom SQS with $A_{0.5}B_{0.5}$ composition and its complementary $B_{0.5}A_{0.5}$ spin configuration. The band gap and the TM magnetic moment are reported for CoO in the AFM phase and the PM phase which was calculated using the displayed 216-atom $3 \times 3 \times 3$ SQS.

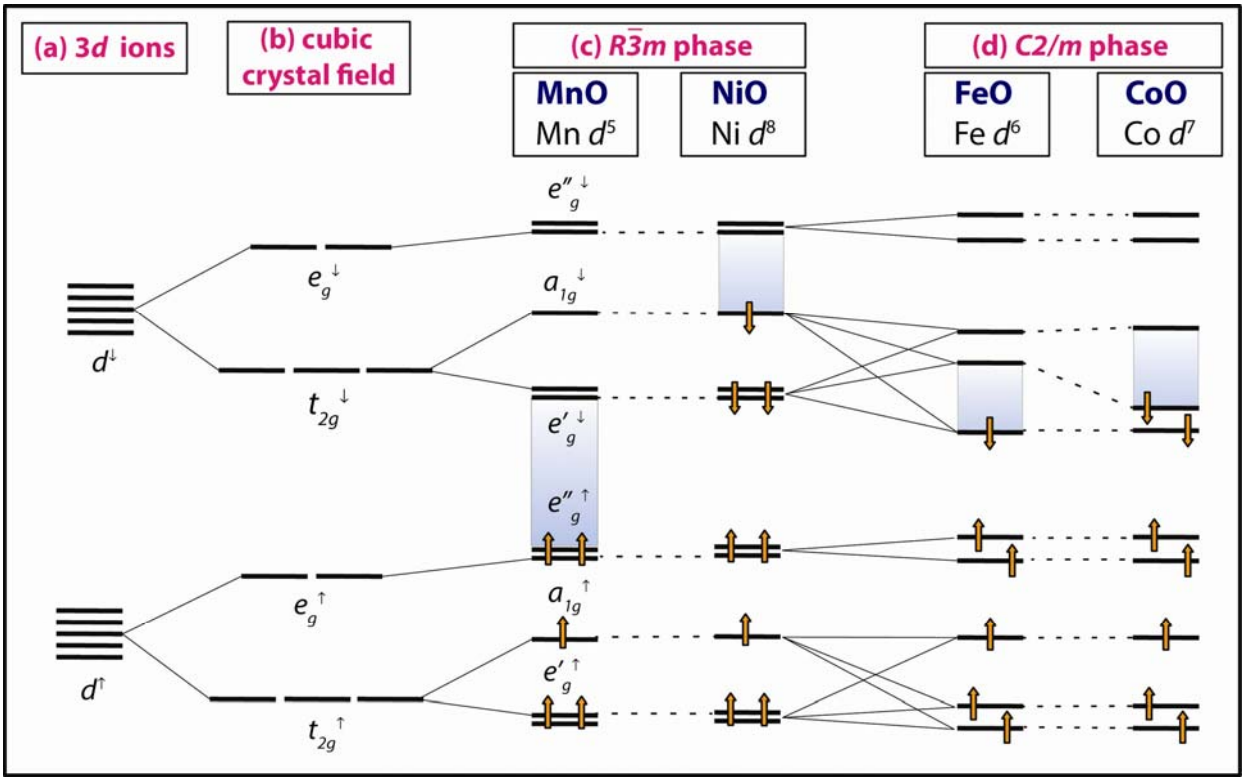

Figure 2. Schematic of the sequence of level splittings and combinations for the *d* orbitals in MnO, NiO, FeO, and CoO as the exchange coupling and the crystal field of the symmetry appropriate to each phase are progressively imposed: (a) Splitting of the *d* orbitals into the transition-metal atoms subjected to exchange coupling. (b) Splitting of the spin-up and spin-down *d* levels subjected to a cubic O_h crystal field: this is the case of a rock salt structure with hypothetical $Fm\bar{3}m$ magnetic ordering. (c) Splitting of the *d* level in the D_{3d} crystal field in the distorted rock-salt lattice with the rhombohedral $R\bar{3}m$ AFM-II magnetic ordering. (d) Splitting of the *d* orbitals in a tetragonal crystal field as in the monoclinic $C2/m$ phases of FeO and CoO. Note that in this schematic we emphasize the effect of the relevant interaction in progressively removing the degeneracy of the *d* orbitals, while we do not intend to reproduce to scale the position of the spin-up and spin-down energy levels. The reader should inspect the projected DOSs of Fig. 3 and 4 to obtain the actual calculated energy position of the *d* bands.

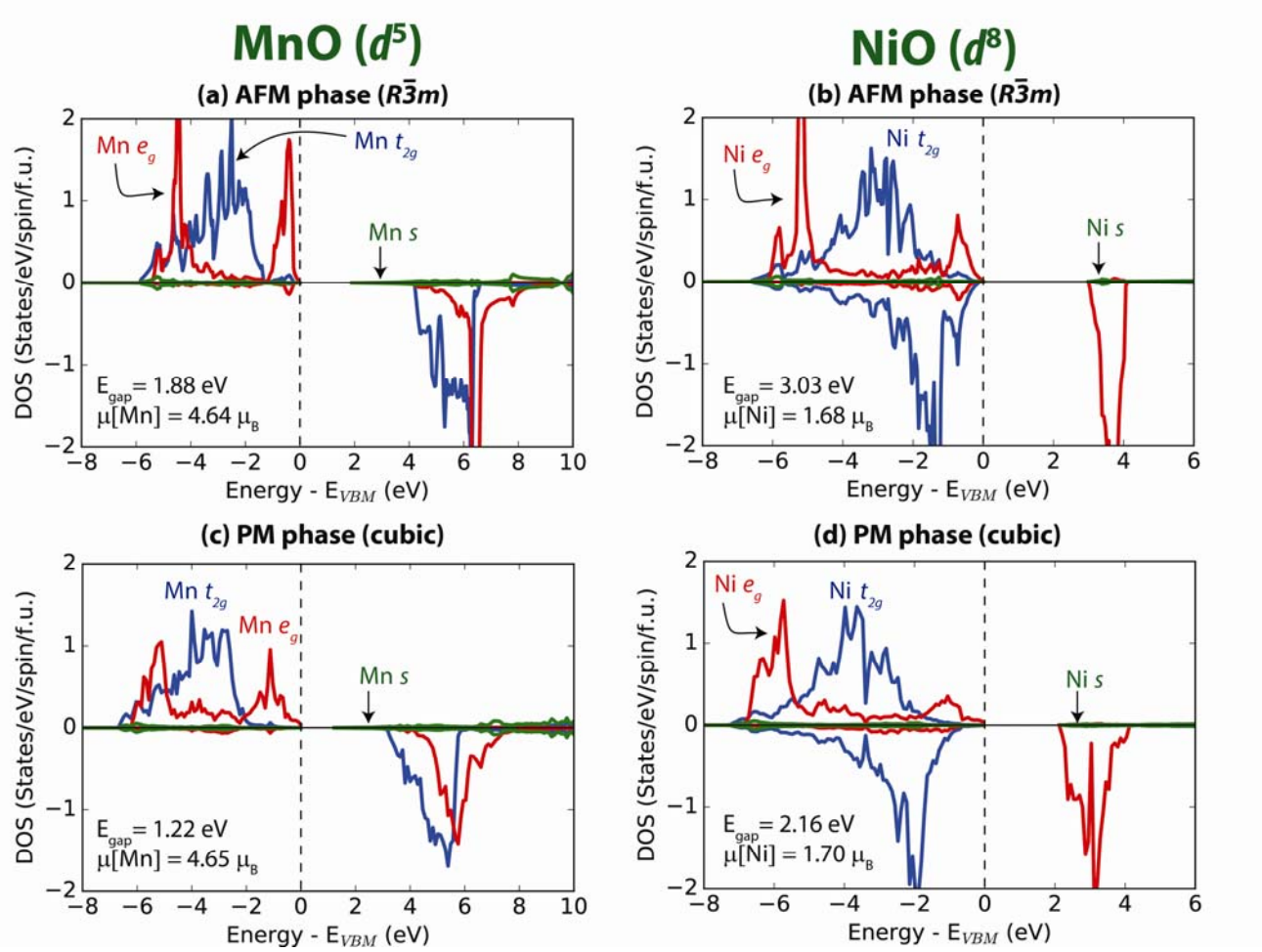

Figure 3. Projected density of states (PDOS) on the transition metal *s* and *d* orbitals (t_{2g} and e_g components) calculated by DFT+*U* (*U*=5 eV) for MnO and NiO in (a)-(b) the AFM phase with fully relaxed $R\bar{3}m$ structures, and (c)-(d) the PM phase modeled by a cubic 64-atom $2 \times 2 \times 2$ SQS. The lattice parameters of the SQSs are set so that the volume per formula unit is equal to the calculated volume per formula unit of the DFT+*U* relaxed $R\bar{3}m$ structures of MnO and NiO.

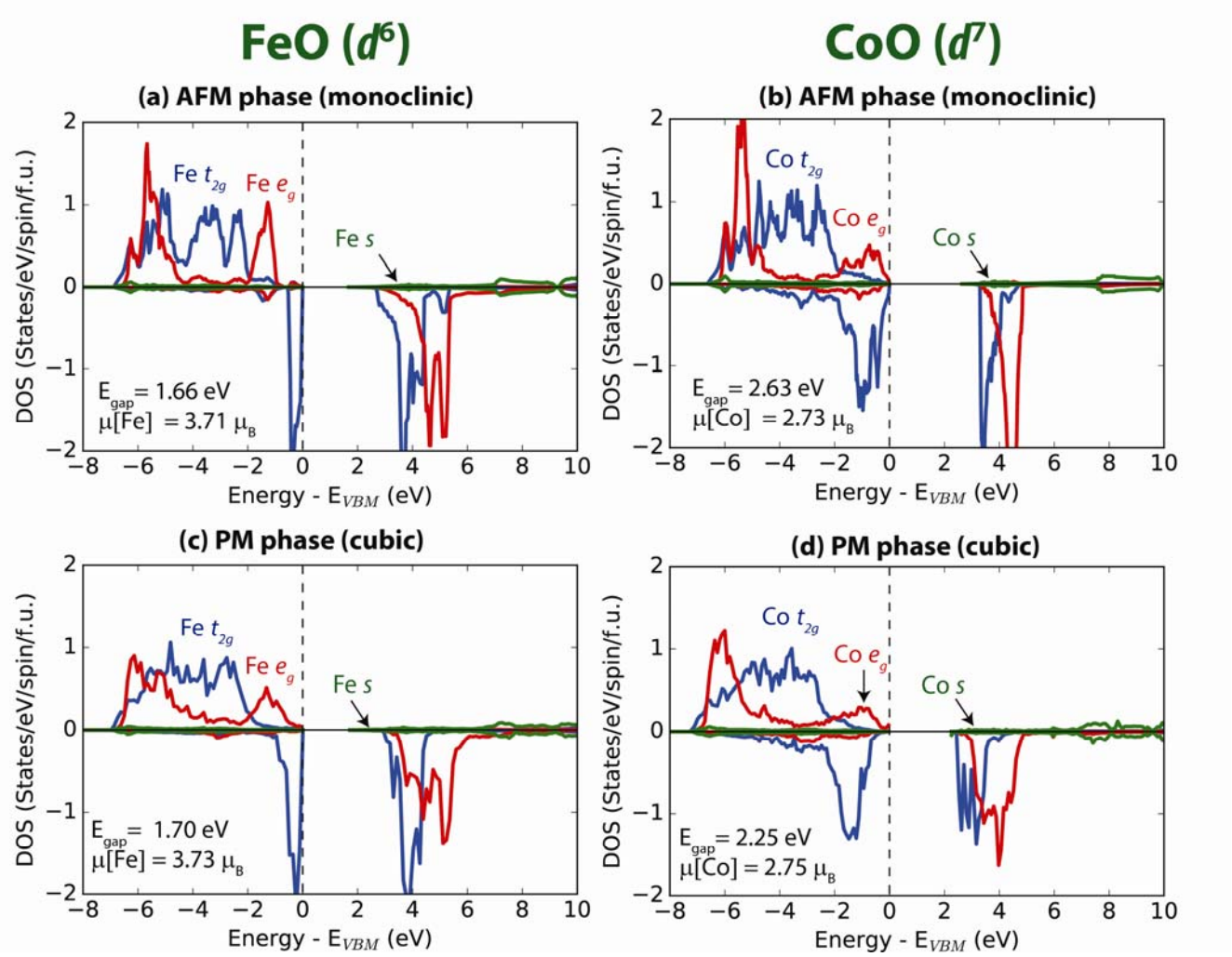

Figure 4. Projected density of states (PDOS) on the transition metal *s* and *d* orbitals (t_{2g} and e_g components) calculated by DFT+*U* (*U*=5 eV) for FeO and CoO in (a)-(b) the AFM phases with the fully relaxed monoclinic $C2/m$ structures, and (c)-(d) the paramagnetic phases modeled by a cubic 64-atom $2 \times 2 \times 2$ SQS. The lattice parameters of the SQSs are set so that the volume per formula unit is equal to the calculated volume per formula unit of the DFT+*U* relaxed $C2/m$ structures of FeO and CoO.

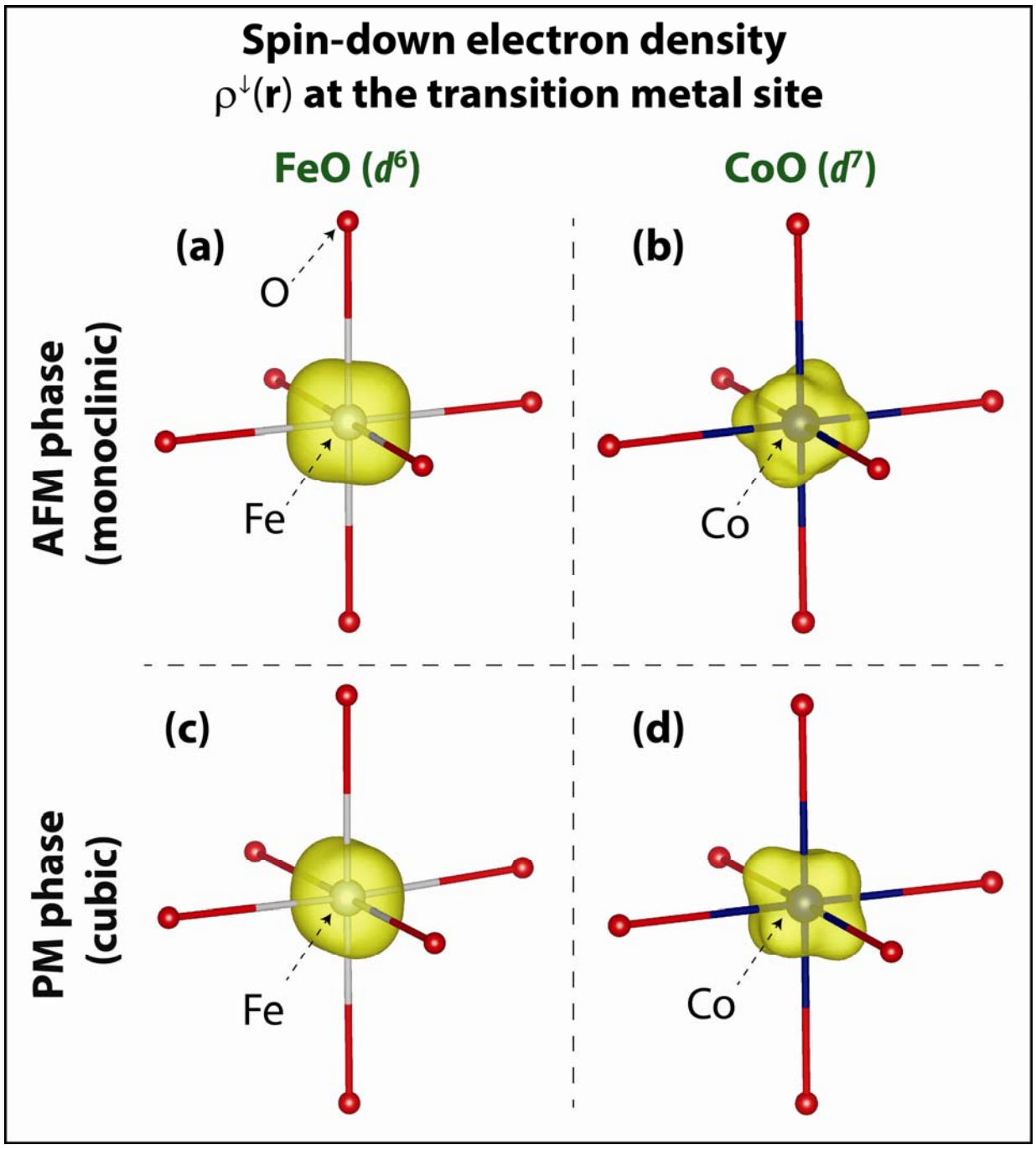

Figure 5. Panel (a) and (b) depict the minority spin electron density $\rho^{\downarrow}(\boldsymbol{r})$ at the Fe and Co site in the AFM monoclinic phases of, respectively, FeO and CoO calculated by DFT+*U*. Panel (c) and (d) depict the minority spin electron density $\rho^{\downarrow}(\boldsymbol{r})$ at the Fe and Co site in the PM phase of, respectively, FeO and CoO modeled by the magnetic 64-atom cubic SQS used for the calculation of the PDOS shown in Fig. 5(c,d). The full $\rho^{\downarrow}(\boldsymbol{r})$ of PM FeO and CoO in the SQS is shown in Fig. 6(a,b).

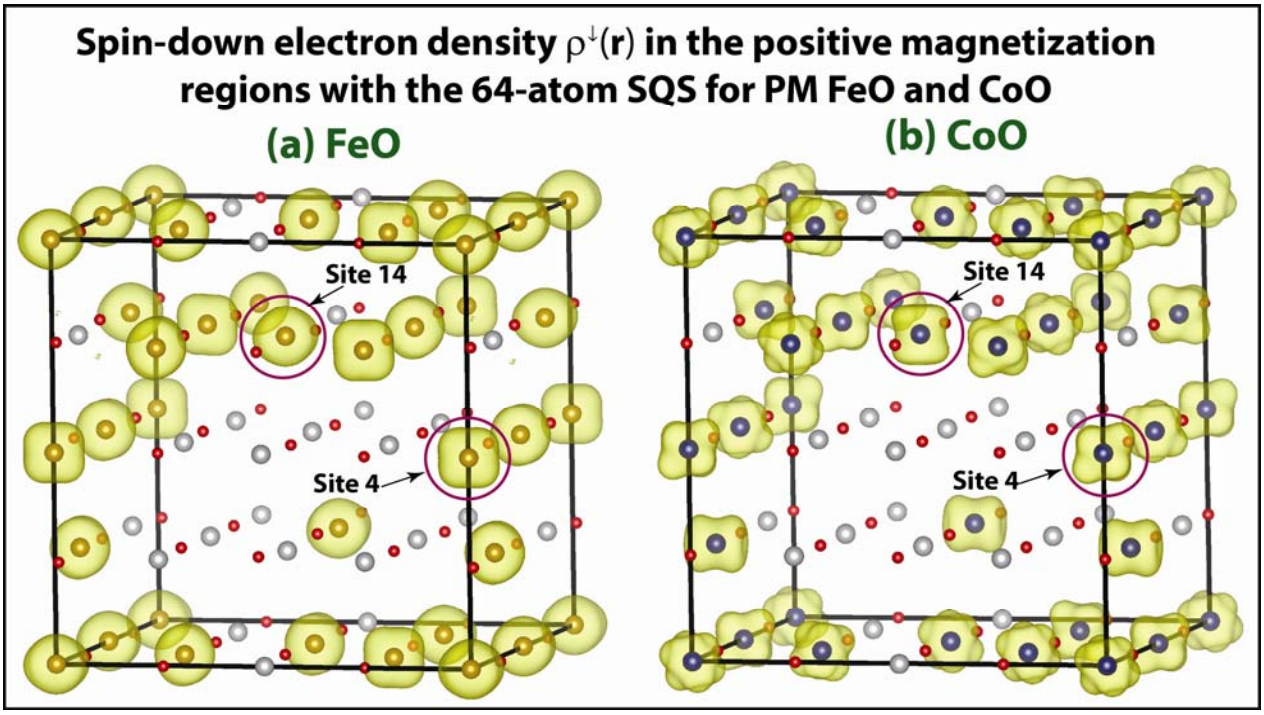

Figure 6. Minority spin electron density $\rho^{\downarrow}(\boldsymbol{r})$ in the regions with positive magnetization $m(r) = \rho^{\uparrow}(\boldsymbol{r}) - \rho^{\downarrow}(\boldsymbol{r}) > 0$ within the magnetic 64-atom SQS cell used in the DFT+U (U=5 eV) calculations of the PM phases of (a) FeO and (b) CoO. To avoid visual clutter we masked out the regions of space within spheres of 1 Å of radius centered at the oxygen sites.

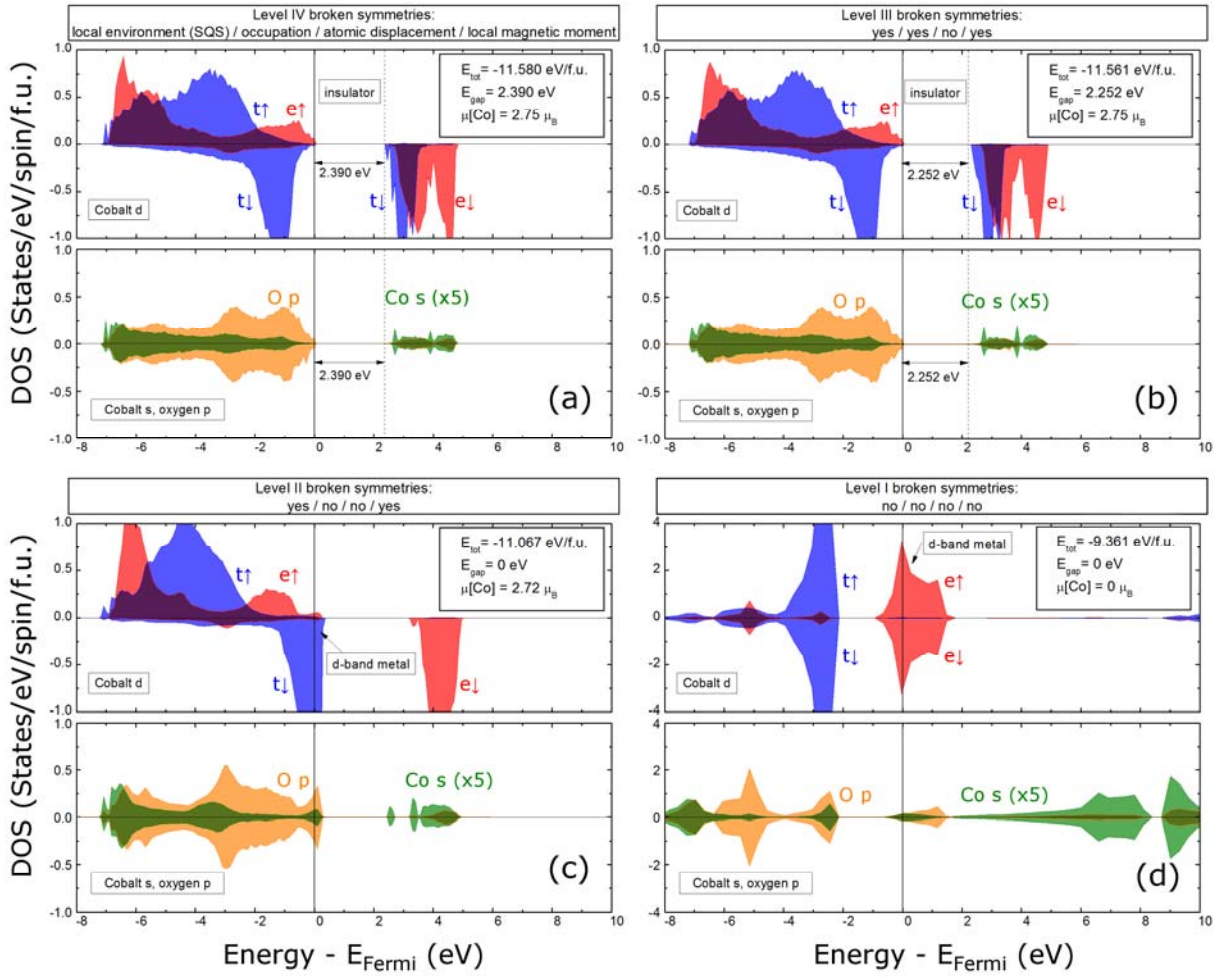

Figure 7. Analysis of the effects of different symmetry breaking modes on the electronic structure, total energy, band gap and local moment of paramagnetic CoO. We show the projected density of states (PDOS) on the transition metal *s* and *d* orbitals (and components) and oxygen *p* orbitals from (a) level IV, (b) level III, (c) level II and (d) level I (see Sec.VII.A for definition of these symmetry breaking levels) of rock salt CoO . (a), (b) and (c) are calculated in a 216-atom cubic rock salt supercell with SQS, while (d) is calculated in a 2-atom rock salt primitive cell. All lattice parameters are the same as the one used in Fig. 4(d).

1. N. F. Mott and Z. Zinamon, Reports on Progress in Physics **33** (3), 302-302 (1970).
2. L. F. Mattheiss, Physical Review B **5** (2), 290-306 (1972).
3. L. F. Mattheiss, Physical Review B **5** (2), 306-315 (1972).
4. X. Ren, I. Leonov, G. Keller, M. Kollar, I. Nekrasov and D. Vollhardt, Physical Review B **74** (19), 195114-195114 (2006).
5. F. Rivadulla, M. Ba?obre-L?pez, C. X. Quintela, A. Pi?eiro, V. Pardo, D. Baldomir, M. A. L?pez-Quintela, J. Rivas, C. A. Ramos, H. Salva, J.-S. Zhou and J. B. Goodenough, Nature Materials **8** (12), 947-951 (2009).
6. B. Alling, T. Marten and I. A. Abrikosov, Nat Mater **9** (4), 283-284 (2010).
7. I. A. Abrikosov, A. V. Ponomareva, P. Steneteg, S. A. Barannikova and B. Alling, Current Opinion in Solid State and Materials Science **20** (2), 85-106 (2016).
8. N. W. Ashcroft and N. Mermin, *Solid State Physics*. (Holt, Rinehart, and Winston, New York, NY, 1976).
9. C. Kittel, *Introduction to Solid State Physics*. (John Wiley & Sons, Inc., 2005).
10. S. Lany, Phys. Rev. B **87** (8), 85112-85112 (2013).
11. I. D. Hughes, M. Däne, A. Ernst, W. Hergert, M. Lüders, J. B. Staunton, Z. Szotek and W. M. Temmerman, New Journal of Physics **10** (6), 063010-063010 (2008).
12. A. Schrön, C. Rödl and F. Bechstedt, Physical Review B **86** (11), 115134-115134 (2012).
13. J. Hubbard, Proceedings of the Royal Society of London A: Mathematical, Physical and Engineering Sciences **276** (1365) (1963).
14. J. Hubbard, Proceedings of the Royal Society of London A: Mathematical, Physical and Engineering Sciences **281**, 481 (1964).
15. A. Georges, W. Krauth and M. J. Rozenberg, Reviews of Modern Physics **68** (1), 13-125 (1996).
16. G. Kotliar, S. Y. Savrasov, K. Haule, V. S. Oudovenko, O. Parcollet and C. A. Marianetti, Reviews of Modern Physics **78** (3), 865-951 (2006).
17. Y. Shinohara, S. Sharma, S. Shallcross, N. N. Lathiotakis and E. K. Gross, Journal of chemical theory and computation **11** (10), 4895-4899 (2015).
18. J. Kuneš, V. I. Anisimov, A. V. Lukoyanov and D. Vollhardt, Physical Review B **75** (16) (2007).
19. S. Biermann, A. Poteryaev, A. I. Lichtenstein and A. Georges, Physical Review Letters **94** (2), 026404 (2005).
20. V. I. Anisimov, J. Zaanen and O. K. Andersen, Physical Review B **44** (3), 943-954 (1991).
21. A. I. Liechtenstein, V. I. Anisimov and J. Zaanen, Physical Review B **52** (8), R5467-R5470 (1995).
22. V. I. Anisimov, F. Aryasetiawan and A. I. Lichtenstein, Journal of Physics: Condensed Matter **9** (4), 767-808 (1997).
23. M. Cococcioni and S. de Gironcoli, Physical Review B **71** (3), 35105-35105 (2005).
24. B. Himmetoglu, A. Floris, S. de Gironcoli and M. Cococcioni, International Journal of Quantum Chemistry **114** (1), 14-49 (2014).
25. S. Lany, J. Osorio-Guillén and A. Zunger, Physical Review B **75** (24) (2007).
26. J. Varignon, M. N. Grisolia, J. Íñiguez, A. Barthélémy and M. Bibes, npj Quantum Materials **2** (1) (2017).
27. F. Zuo, P. Panda, M. Kotiuga, J. Li, M. Kang, C. Mazzoli, H. Zhou, A. Barbour, S. Wilkins, B. Narayanan, M. Cherukara, Z. Zhang, S. Sankaranarayanan, R. Comin, K. M. Rabe, K. Roy and S. Ramanathan, Nature communications **8** (1), 240 (2017).
28. A. Walsh and A. Zunger, Nature Materials **16**, 964 (2017).

29. J. P. Perdew and A. Zunger, Physical Review B **23** (10), 5048-5079 (1981).
30. J. Heyd, G. E. Scuseria and M. Ernzerhof, The Journal of Chemical Physics **118** (18), 8207-8215 (2003).
31. C. Franchini, G. Kresse and R. Podloucky, Phys. Rev. Lett. **102** (25), 256402-256402 (2009).
32. M. Retuerto, T. Emge, J. Hadermann, P. W. Stephens, M. R. Li, Z. P. Yin, M. Croft, A. Ignatov, S. J. Zhang, Z. Yuan, C. Jin, J. W. Simonson, M. C. Aronson, A. Pan, D. N. Basov, K. G and M. Greenblatt, Chemistry of Materials **25** (20), 4071-4079 (2013).
33. F. Ducastelle, *Order And Phase Stability in Alloys*. (North-Holland, Amsterdam, 1991).
34. R. Magri, S. H. Wei and A. Zunger, Physical Review B **42** (17), 11388-11391 (1990).
35. C. Wolverton and A. Zunger, Physical Review B **51** (11), 6876-6891 (1995).
36. Z. W. Lu, S. H. Wei, A. Zunger, S. Frota-Pessoa and L. G. Ferreira, Phys. Rev. B **44**, 512-544 (1991).
37. Z. W. Lu, S. H. Wei and A. Zunger, Physical Review B **44** (19), 10470-10484 (1991).
38. Z. W. Lu, S. H. Wei and A. Zunger, Physical Review B **45** (18), 10314-10330 (1992).
39. C. Wolverton and A. Zunger, Physical Review Letters **75** (17), 3162-3165 (1995).
40. Y. Wang, G. M. Stocks, W. A. Shelton, D. M. C. Nicholson, Z. Szotek and W. M. Temmerman, Physical Review Letters **75** (15), 2867-2870 (1995).
41. L. Vitos, I. A. Abrikosov and B. Johansson, Physical Review Letters **87** (15), 156401-156401 (2001).
42. A. Zunger, S. H. Wei, L. G. Ferreira and J. E. Bernard, Physical Review Letters **65** (3), 353-356 (1990).
43. S. H. Wei, L. G. Ferreira, J. E. Bernard and A. Zunger, Physical Review B **42** (15), 9622-9649 (1990).
44. A. van de Walle, M. Asta and G. Ceder, Calphad **26**, 539-539 (2002).
45. A. van de Walle, Calphad **33**, 266-266 (2009).
46. A. van de Walle, P. Tiwary, M. M. de Jong, D. L. Olmsted, M. D. Asta, A. Dick, D. Shin, Y. Wang, L. Q. Chen and Z. K. Liu, Calphad **42**, 13-13 (2013).
47. A. Baldereschi, Physical Review B **7** (12), 5212-5215 (1973).
48. D. J. Chadi and M. L. Cohen, Physical Review B **8** (12), 5747-5753 (1973).
49. K. C. Hass, L. C. Davis and A. Zunger, Physical Review B **42** (6), 3757-3760 (1990).
50. B. Dorado and P. Garcia, Physical Review B **87** (19) (2013).
51. B. Alling, T. Marten and I. A. Abrikosov, Physical Review B **82** (18) (2010).
52. P. Larson, W. R. L. Lambrecht, A. Chantis and M. van Schilfgaarde, Physical Review B **75** (4) (2007).
53. B. Dorado, B. Amadon, M. Freyss and M. Bertolus, Physical Review B **79** (23) (2009).
54. B. Meredig, A. Thompson, H. A. Hansen, C. Wolverton and A. van de Walle, Physical Review B **82** (19) (2010).
55. S. L. Dudarev, G. A. Botton, S. Y. Savrasov, C. J. Humphreys and A. P. Sutton, Phys. Rev. B **57**, 1505-1509 (1998).
56. H. J. Kulik, M. Cococcioni, D. A. Scherlis and N. Marzari, Physical review letters **97** (10), 103001-103001 (2006).
57. G. Kresse and J. Furthmu□ller, Comput. Mater. Sci. **6**, 15-50 (1996).
58. G. Kresse and D. Joubert, Phys. Rev. B **59**, 1758-1775 (1999).
59. J. P. Perdew, K. Burke and M. Ernzerhof, Physical Review Letters **77** (18), 3865-3868 (1996).
60. A. Franceschetti, S. V. Dudiy, S. V. Barabash, A. Zunger, J. Xu and M. van Schilfgaarde, Physical Review Letters **97** (4), 047202 (2006).
61. M. Däne, M. Lüders, A. Ernst, D. Ködderitzsch, W. M. Temmerman, Z. Szotek and W. Hergert, Journal of physics: Condensed matter **21** (4), 045604-045604 (2009).
62. I. I. Mazin and V. I. Anisimov, Physical Review B **55** (19), 12822-12825 (1997).

63. J. P. Allen and G. W. Watson, Phys. Chem. Chem. Phys. **16** (39), 21016-21031 (2014).
64. K. Terakura, A. R. Williams, T. Oguchi and J. Kübler, Physical Review Letters **52** (20), 1830-1833 (1984).
65. K. Terakura, T. Oguchi, A. R. Williams and J. Kübler, Physical Review B **30** (8), 4734-4747 (1984).
66. R. Gillen and J. Robertson, Journal of physics. Condensed matter : an Institute of Physics journal **25** (16), 165502-165502 (2013).
67. A. Svane and O. Gunnarsson, Physical review letters **65** (9), 1148-1151 (1990).
68. J. Goodenough, Progress in Solid State Chemistry **5**, 145-399 (1971).
69. S. Saito and Y. Nakahigashi Kiyotaka Shimomura, J. Phys. Soc. Jpn. **21** (5), 850-850 (1966).
70. W. Jauch, M. Reehuis, H. J. Bleif, F. Kubanek and P. Pattison, Physical Review B **64** (5), 052102-052102 (2001).
71. H. Fjellvag, B. C. Hauback, T. Vogt and S. Stolen, American Mineralogist **87** (511), 347-347 (2002).
72. F. Gehbard, *The Mott Metal-Insulator Transition, Models and Methods*. (Springer-Verlag Heidelberg, 1997).
73. S. Biermann, (2014), pp. 303-345.
74. H. Hasegawa, Journal of the Physical Society of Japan **46**, 1504-1514 (1979).
75. J. Hubbard, Physical Review B **20** (11), 4584-4595 (1979).
76. J. Hubbard, Physical Review B **19** (5), 2626-2636 (1979).
77. B. L. Gyorffy, A. J. Pindor, J. Staunton, G. M. Stocks and H. Winter, Journal of Physics F: Metal Physics **15** (6), 1337-1386 (1985).
78. K. A. Maeder and A. Zunger, Physical Review B **51** (16), 10462-10476 (1995).
79. K. Momma and F. Izumi, Journal of Applied Crystallography **44** (6), 1272-1276 (2011).